# Formation and dynamics of bubbles in breaking waves: Part I. Algorithms for the identification of bubbles and breakup/coalescence events

By W. H. R. Chan, M. S. Dodd, P. L. Johnson, J. Urzay and P. Moin

#### 1. Motivation and objectives

Breaking waves in oceans generate bubbles of a wide range of scales, which in turn influence interfacial mass, momentum and energy transfer processes (Thorpe 1992; Melville 1996), surface reflectance (Terrill et al. 2001; Reed & Milgram 2002; Zhang et al. 2004; Seitz 2011; Crook et al. 2016), and the propagation of acoustic waves (Pumphrey & Crum 1988; Trevorrow et al. 1994; Stanic et al. 2009). Numerous experiments have been devised to measure bubble populations as a function of bubble size due to breaking waves generated under a wide variety of conditions. Of these, the experiments by Deane & Stokes (2002) and Blenkinsopp & Chaplin (2010) were able to measure bubbles over a size range spanning more than two decades (between 100 µm and 10 mm) within a single experimental setup—one of the largest size ranges of simultaneously-measured bubbles to date. While there are differences in the bubble size distributions reported in both works due to the different wave parameters and measurement techniques used, as well as the stage of wave breaking during which the measurements were obtained, there seem to be two common themes in the resulting measurements: first, the distribution of the larger bubbles appears to scale differently from the distribution of the smaller bubbles; second, these distributions evolve significantly in time as the wave breaks. Similar observations have been made in recent numerical simulations of breaking third-order Stokes waves by Wang et al. (2016) and Deike et al. (2016). It appears, then, that different physical mechanisms are at play at different length and time scales in the formation and dynamics of bubbles in these breaking waves. These mechanisms have not been straightforward to isolate and are a subject of active research.

As previously noted (Chan et al. 2016, 2017, 2018a), the cost of direct numerical simulation of turbulent breaking waves with realistic amplitudes and wavelengths is prohibitive due to the wide range of scales involved, necessitating the development of subgrid-scale (SGS) models to enable the large eddy simulation of these flows. A physics-based SGS model demands a fundamental understanding of the breakup and coalescence processes leading to the development and subsequent evolution of the bubble size distribution near and below the grid scale. With this goal in mind, an ensemble of simulations of breaking Stokes waves of a smaller amplitude and wavelength is employed to better understand these processes at the scales resolvable for these waves, in the hope that physical insights at the smaller length scales to be modeled may eventually be elucidated for more energetic waves. The current status of this work is documented in two research briefs: in the first (present) brief, algorithms to identify bubbles and to detect bubble breakup and coalescence events in a two-phase simulation with knowledge of the volume fraction

field are detailed. In the second brief (Chan et al. 2018b), these algorithms are used to characterize the evolution of the bubble size distribution in the aforementioned ensemble, including the identification of breakup and coalescence events. Then, on the basis of trends observed in the evolution of the distribution and accompanying events, a pathway for the identification of potential mechanisms for bubble breakup and coalescence is outlined.

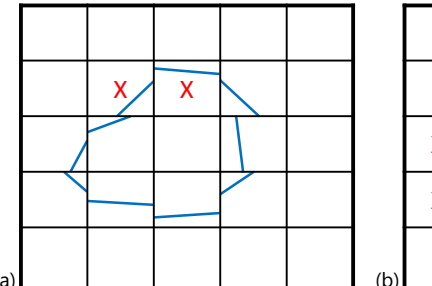
This brief is organized as follows: in Section 2, several algorithms used to compute bubble size distributions in two-phase simulations with knowledge of the volume fraction field are discussed and compared for a simple test case (single drop) and a complex flow field (breaking wave). In Section 3, an algorithm that detects breakup and coalescence events by tracking bubble centroids and volumes is detailed with a demonstration case (two-phase Taylor-Green vortex). Closing remarks on the various algorithms are provided in Section 4. A discussion of the evolution of these distributions and the occurrence of these events as gleaned from applying these algorithms to the breaking wave simulation ensemble is deferred to the companion brief (Chan et al. 2018b).

## 2. Bubble identification algorithms for bubble size distribution computation

### 2.1. The traditional flood-fill algorithm as used in bubble identification

The traditional method for identifying bubbles in an interface-capturing or interfacetracking scheme where the volume fraction of each phase in each computational cell—or node in a node-centered code—is either immediately known or reconstructible is based on the flood-fill algorithm, which is also used in raster graphic editors to color connected areas. The exact mechanics of filling depend on whether the algorithm is implemented in a stack-based (recursive) or queue-based (nonrecursive) fashion looping over each cell, or with a multiple-queue-based (nonrecursive) approach looping over pairs of cells. To the best of the authors' knowledge, the algorithms used by Wang et al. (2016) and Deike et al. (2016) perform the loop over each cell, while the algorithm implemented in this work performs the loop over pairs of nodes (Kim et al. 2014). No difference in the final result is expected between the various implementations. Once the filling is complete, the algorithm yields contiguous groups of computational cells, where each group here is deemed to be a bubble. The flood-fill algorithm guarantees that every cell in each contiguous group is a neighbor of at least one other cell in the same group such that this pair of cells satisfies a predetermined criterion. To obtain contiguous groups of cells corresponding to bubbles in an air-water system, the selected criterion here might be that a pair of neighboring cells is added to a group already containing at least one of the cells—or a new group, if there are no such existing groups—if both cells contain nonzero amounts of air. Mathematically, if two neighboring cells i and j have air volume fractions  $\phi_i$  and  $\phi_j$ , then they are added to the group defined above if  $\phi_i, \phi_i > \phi_c$ , where the threshold air volume fraction  $\phi_c = 0$ . This grouping process is illustrated in Figure 1 in the context of the volume-of-fluid (VoF) scheme adopted in the code used in this work (Kim et al. 2014), but may be generalized to other interface-capturing and interface-tracking schemes if the volume fraction in each computational cell may be reconstructed.

Because of its relative simplicity, the aforementioned bubble identification algorithm is generally not expected to fail, except in the case where energetic impacts and turbulent eddies create pinch-off events that may result in the formation of very small closely spaced wisps of air. Each of these wisps corresponds to a single computational cell (or node) containing a very small volume fraction of air. These wisps are possibly suppressed in



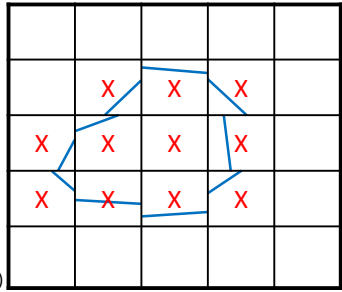


FIGURE 1. Schematics illustrating the flood-fill algorithm as applied to the identification of bubbles in an air-water system simulated by a volume-of-fluid (VoF)-based two-phase solver. Each box in each grid corresponds to a single computational cell (median dual cell in the case of a node-centered code), and each of the diagonal lines occupying the interior of some of these cells corresponds to a planar numerical interface (here linear in a two-dimensional projection) as is typical in piecewise linear interface calculation VoF schemes. Suppose that in each of these divided cells, the portion closer to the center of the subfigure contains air and the other portion contains water. Then, the volume approximately bounded by the entire set of these interfaces should constitute a bubble. (a) The pair of crosses highlights a pair of neighboring cells that satisfies the grouping criterion in Section 2.1 that both cells contain nonzero amounts of air, or one of the alternative criteria listed in Section 2.2. (b) The crosses highlight all the cells each of which belongs to at least one cell pair satisfying this grouping criterion. This contiguous collection of cells will be identified by the flood-fill algorithm as a single bubble.

split VoF advection schemes [e.g., Scardovelli & Zaleski (2003), Weymouth & Yue (2010), Baraldi et al. (2014) and Fuster et al. (2018), where redistribution or dilatational fluxes are employed to avoid overfilling or over-emptying of cells, and may occur more frequently in unsplit schemes where it is unnecessary to employ these fluxes to maintain volume conservation. When these wisps occur, it is possible that a large collection of these air wisps will be neighboring, leading to them being grouped together and identified as a single large bubble by this algorithm, even though they may not necessarily correspond to a single bubble in a physical wave. One such spurious bubble identified in one of the breaking wave simulations performed in this work [see Chan et al. (2018a) and Section 2.4] is depicted in Figure 2. Note that in this example, the volume fraction of air in many of these cells is between  $10^{-3}$  and  $10^{-4}$ , and thus larger than typical machineprecision errors. (See, also, the fourth row of Table 1.) Large spurious bubbles may contain sufficiently large volumes of air to appear in the instantaneous bubble size distribution at resolvable radii and thus introduce errors in the distribution. These errors will be further discussed in Section 2.4. Accurate reporting of bubble size distributions in two-phase numerical simulations, especially of flows with energetic impacts and turbulent eddies, then demands the exclusion of these spurious bubbles through the modification of the employed bubble identification method, and in particular the grouping criterion used for the pairwise cell (or node) evaluation.

#### 2.2. Modifying the pairwise evaluation criterion in the flood-fill algorithm

The original grouping criterion suggested above (denoted Scheme A in the subsequent discussion)—that both cells in the cell pair being considered contain nonzero amounts of air—artificially chains closely spaced cells with very small volume fractions of air together. Alternative grouping criteria, such as the following, may be considered to eliminate this corner case. First, one may exclude computational cells containing small volume fractions of air (clipping, denoted Scheme B in subsequent figures and tables with a specific choice

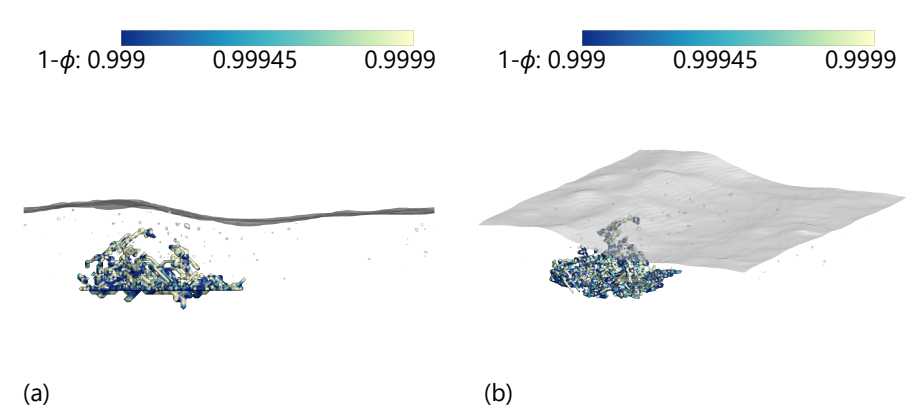


FIGURE 2. Locations of nodes that were identified as part of a spurious air bubble detected using a naive application of the flood-fill algorithm (grouping criterion of Section 2.1) on a snapshot of a Stokes water wave simulation after breaking. The perimeter nodes of the spurious bubble are shaded by the volume fraction of water  $(1-\phi)$  at each computational node. (a,b) The same spurious bubble from different view angles. The light and smooth translucent surfaces in the subfigures represent the  $\phi = 0.5$  isosurface of the wave. The parameters of this simulation are available in a publication by Chan *et al.* (2018a) and Section 2.4. These snapshots were obtained at a nondimensional time  $t^* = 11.8$ , well after the first impact at about  $t^* = 1.2$ .

of  $\phi_c$ ). In order for cells to be considered in the grouping algorithm under this criterion, their air volume fraction should be above a certain threshold  $\phi_c > 0$ . A sufficiently large threshold will prevent spurious bubbles involving small wisps of air from being identified, but will also numerically clip the volumes of larger bubbles whose boundaries are likely composed of some cells with small air volume fractions. This is due to the inherent nature of volume discretization: if the surface of the bubble volume does not conform to the underlying mesh geometry, then cut cells of a wide range of air volume fractions are almost certain to be generated where the surface intersects with the mesh. Second, one may only include computational cells directly associated with a large mass of air (substantial mass test, Scheme C). In order for a pair of cells to be considered in the grouping algorithm under this criterion, at least one of the cells should have an air volume fraction above a certain threshold  $\phi_{c,m} > 0$ . Physically, small wisps of air are only considered for grouping if they are attached to a large mass of air. The corner case of this criterion (see, also, the penultimate row of Table 1) is that if two large masses of air are connected by a thin air bridge in a single cell with a small air volume fraction, then they will be grouped by the algorithm as a single bubble. Third, one may only include computational cells indirectly associated with a large mass of air (substantial neighbor test, Scheme D). In order for a pair of cells to be considered in the grouping algorithm under this criterion, at least one of the cells should have one neighbor (or more) with an air volume fraction above a certain threshold  $\phi_{c,n} > 0$ , or itself satisfy this condition. This also restricts small wisps of air to be considered for grouping only if they are attached to a large mass of air. The corner case of this criterion (see, also, the last row of Table 1) is that if two large masses of air are connected by a thin air bridge that is one cell wide and two cells long (or two small bubbles each taking up one cell), then they will be grouped by the algorithm as a single bubble. Note that the corner cases of the substantial mass and neighbor tests do not necessarily indicate deficiencies of the schemes, but rather are representative of an inherent limitation of a VoF field with finite

Case				Scheme A	Scheme B	Scheme C	Scheme D
0.85	1.00	1.00	0.44		_	_	_
0.15	0.49	0.32	0.09				
0.00	0.00	0.00	0.00				
0.85	1.00	1.00	0.44			_	_
0.15	0.49	0.32	0.09		X		
0.00	0.00	0.00	0.00				
0.85	1.00	1.00	0.44				
0.15	0.49	0.32	0.09		X	X	
0.00	0.00	0.00	0.00				
10-3	10-3	10-5	10-3				
10-4	10-4	10-3	10-3		X	X	X
10-3	10-3	10-4	10-3				
0.15	0.00	0.52	1.00				
0.85	0.49	0.93	1.00		X		
0.92	0.00	0.81	1.00				
0.15	0.00	0.00	0.52				
0.85	0.31	0.49	0.93		X	X	$\checkmark$
0.92	0.00	0.00	0.81				
		ı	1				

Table 1. Pairs of cells that are permitted (checkmark)/not permitted (cross) for inclusion in the grouping algorithm subject to the various grouping criteria: original criterion in Section 2.1 (Scheme A), clipping (Scheme B) with  $\phi_c = 0.5$ , substantial mass test (Scheme C) with  $\phi_{c,m} = 0.5$ , and substantial neighbor test (Scheme D) with  $\phi_{c,n} = 0.5$ . Each row in the table corresponds to a particular pair of cells, depicted together with some of its neighbors, in the first column. For an explanation of the grid and lines in each subfigure, refer to the caption of Figure 1. The numbers in each cell correspond to the local volume fraction of air. The two cells under consideration have their volume fractions in black; the other cells have their volume fractions in gray. The volume fraction field in the first three rows of the table is identical, with different cell pairs highlighted in each row.

resolution: when a thin air bridge is indistinguishable from a small, underresolved bubble or a small air protrusion with no additional information available, none of the geometries necessarily represent reality more accurately, and any decision by any scheme to favor any of the geometries is consequently arbitrary to a certain degree.

Table 1 illustrates the types of volume fraction pairs that are permissible for grouping

Scheme	Volume error/ $\Delta^3$ $(D/\Delta = 8)$	Centroid error/ $\Delta$ $(D/\Delta = 8)$	Volume error/ $\Delta^3$ $(D/\Delta = 16)$	Centroid error/ $\Delta$ $(D/\Delta = 16)$
В1	$27\pm2$	$(2\pm1)\times10^{-2}$	$101 \pm 4$	$(1.3 \pm 0.8) \times 10^{-2}$
B2	$2.4 \pm 0.3$	$(5\pm 2)\times 10^{-3}$	$8.8 \pm 0.5$	$(2\pm1)\times10^{-3}$
С	$(4 \pm 3) \times 10^{-2}$	$(3\pm 2)\times 10^{-4}$	$(8 \pm 3) \times 10^{-2}$	$(1.3 \pm 0.8) \times 10^{-4}$
D	$(5 \pm 6) \times 10^{-7}$	$(7 \pm 7) \times 10^{-9}$	$(2\pm1)\times10^{-6}$	$(4\pm 2) \times 10^{-9}$

Table 2. Nondimensional volume and centroid location errors for the case of the drop advected with an imposed velocity. In each entry, the first value refers to the mean absolute deviation from the ground truth, while the second value refers to the root-mean-square deviation. Here, D denotes the drop diameter and  $\Delta$  denotes the grid spacing. The errors are plotted for the following grouping criteria: clipping with  $\phi_c = 0.5$  (Scheme B1), clipping with  $\phi_c = 0.1$  (Scheme B2), substantial mass test (Scheme C) with  $\phi_{c,m} = 0.5$ , and substantial neighbor test (Scheme D) with  $\phi_{c,n} = 0.5$ .

under the constraints of the various grouping criteria above. Generally, and as suggested by the cases considered in Table 1, the volume loss encountered by a large volume due to the culling of cell pairs by the various grouping criteria follows the trend: clipping  $\gtrsim$  substantial mass test  $\gtrsim$  substantial neighbor test; i.e., the first scheme incurs the largest volume error, and the third scheme incurs the smallest (on average). This is shown on a statistical basis in the next subsection.

# 2.3. Comparison of algorithms: single drop

In order to quantitatively compare the errors incurred by the various grouping criteria, the volume and center-of-mass location of a moving water drop in air are evaluated for the various schemes. The drop is moved across the computational domain in two ways: first, the drop is advected with an imposed velocity and without deformation; second, the drop is advected across the domain subject to the solution of the Navier-Stokes (N-S) equations using the solver described by Kim et al. (2014). The former effectively provides samples of the volume and centroid location at different drop positions relative to the mesh, while the latter enables a glimpse of the expected performance of the various schemes closer to a typical use case where there is coupling between the momentum of both phases. The parameters of the latter case are outlined in the caption of Table 3. In both cases, the computational domain selected was cubic and periodic with 5 drop diameters and an equal number of cells along each axis, and all schemes were tested on meshes with 8 and 16 cells across the initial drop diameter. Also, here, the original grouping criterion in Section 2.1 provides the ground truth, so all computed errors are relative to the quantities yielded by the original grouping criterion. Table 2 lists the nondimensional volume and centroid location errors for the various schemes in the case of the drop advected with an imposed velocity, while Table 3 lists the same errors for the drop advected by the solution of the N-S equations. All length scales are normalized by the grid spacing. In these cases, the volume and centroid location errors decrease among the schemes in the following manner: clipping > substantial mass test > substantial neighbor test, as was asserted at the end of Section 2.2. Note, also, that the normalized location errors are much smaller than the normalized volume errors. In addition, the difference between the errors from the case of the drop advected with an imposed velocity and those from the case of the drop advected by the solution of the N-S equations does not seem to be significant.

In an attempt to generalize the computation of the volume error, it is claimed here

Scheme	Volume error/ $\Delta^3$ $(D/\Delta = 8)$	Centroid error/ $\Delta$ $(D/\Delta = 8)$	Volume error/ $\Delta^3$ $(D/\Delta = 16)$	Centroid error/ $\Delta$ ( $D/\Delta = 16$ )
B1	$27\pm2$	$(2\pm1)\times10^{-2}$	$103 \pm 5$	$(1.5 \pm 0.9) \times 10^{-2}$
B2	$2.6 \pm 0.3$	$(5 \pm 2) \times 10^{-3}$	$9.1 \pm 0.8$	$(3\pm1)\times10^{-3}$
С	$(10 \pm 4) \times 10^{-2}$	$(7 \pm 4) \times 10^{-4}$	$(14 \pm 4) \times 10^{-2}$	$(2\pm1)\times10^{-4}$
D	Less than m.p.	Less than m.p.	Less than m.p.	Less than m.p.

Table 3. Nondimensional volume and centroid location errors for the case of the drop advected by the solution of the N-S equations. Refer to the caption of Table 2 for the definitions of the symbols and schemes. Using the initial drop diameter D and velocity U as the characteristic length and velocity scales for the motion of the drop, the initial drop Weber and Stokes numbers may be expressed as  $We = \rho_l U^2 D/\sigma = 25$  and  $St = \rho_l U D/\mu_g = 1.5 \times 10^5$ , respectively, where l denotes liquid and g denotes gas. Here, m.p. denotes machine precision, and "less than m.p." indicates that the computed error is associated with a value less than the standard double precision machine epsilon  $\sim 10^{-16}$ .

that the nondimensional volume error is proportional to the nondimensional surface area bounding the entire volume, and that the constant of proportionality is a function of only the grouping criterion used. This proportionality is demonstrated for a sufficiently large spherical volume with diameter D. Suppose that the only source of volume error is the culling of some of the cut cells at the surface by the grouping criterion (e.g., as suggested by the first three cases in Table 1). The volume error may then be approximated as being proportional to the difference in the volume of the sphere,  $V_1 = \pi D^3/6$ , and the volume of the same sphere slightly enlarged,  $V_2 = \pi (D + \Delta D)^3/6$ , where  $\Delta D$  is on the order of the grid spacing. Assuming  $\Delta D \ll D$ , the volume difference may be written as  $\delta V = V_2 - V_1 \approx \pi D^2 \Delta D/2$ . Correspondingly, the volume error  $\Delta V_{\rm err} \propto \delta V$  may be expressed as

$$\frac{\Delta V_{\rm err}}{(\Delta D)^3} \propto \left(\frac{D}{\Delta D}\right)^2.$$
 (2.1)

One may then write

$$\frac{\Delta V_{\rm err}}{(\Delta D)^3} = M \left[ \pi \left( \frac{D}{\Delta D} \right)^2 \right]$$
 (2.2)

for some constant of proportionality M. It may further be shown that for a sufficiently large spherical volume of size D, the corresponding relative diameter error  $\Delta D_{\rm err}/D$  may be estimated as

$$\frac{\Delta D_{\rm err}}{D} \approx 2M \frac{\Delta D}{D}.$$
 (2.3)

In particular, one may obtain, from Eq. (2.2),  $\Delta V_{\rm err} = M \Delta D \pi D^2 \approx \pi D^2 \Delta D_{\rm err}/2$ .

In Section 3, the principle of mass conservation will be used to determine bubble breakup and coalescence events. This demands that the volume of each bubble be known as accurately as possible from one flow snapshot to another. These breakup and coalescence events may involve one small bubble and one large bubble, but the total volume of air must still be preserved during each event. Denote the diameter of the smaller bubble as d and the diameter of the larger bubble as D. If the volume of the smaller bubble is on the same order as the error in the volume of the larger bubble, then these large-size-ratio events may not be accurately detected after invoking the principle of mass conservation.

Scheme	$D/\Delta = 8)$	$r/\sqrt{N} \\ (D/\Delta = 8)$	$D/\Delta = 16$	$   \begin{array}{c} r/\sqrt{N} \\ (D/\Delta = 16) \end{array} $
B1	0.1	1	0.1	1
B2	0.01	4	0.01	4
С	$2 \times 10^{-4}$	30	$1 \times 10^{-4}$	40
D	$3 \times 10^{-9}$	$8 \times 10^3$	$2 \times 10^{-9}$	$9 \times 10^{3}$

Table 4. Values of M and r as defined in Eqs. (2.2) and (2.5), respectively, for the case of the drop advected with an imposed velocity. Refer to the caption of Table 2 for the definitions of the symbols and schemes. The relative diameter error for each drop and scheme may be obtained by substituting M into Eq. (2.3).

Preempting the discussion in Section 3.1, the critical size ratio  $r \equiv D/d$  where this occurs is of interest. This constraint may be expressed as

$$\frac{\pi \left(\frac{d}{\Delta D}\right)^3}{6} = \frac{\pi N^3}{6} \sim M \left[ \pi \left(\frac{D}{d} \frac{d}{\Delta D}\right)^2 \right] = M \left[ \pi \left(\frac{D}{d} N\right)^2 \right], \tag{2.4}$$

or

$$r = \frac{D}{d} \sim \sqrt{\frac{N}{6M}},\tag{2.5}$$

where  $N \equiv d/(\Delta D)$  is the number of cells across the smaller bubble of diameter d. Observe that  $r/\sqrt{N}$  is a function of only M. Thus, the better the resolution of the smaller bubble, the larger the critical size ratio r.

Returning to the single drop test case, Tables 4 and 5 re-express the volume errors in Tables 2 and 3, respectively, in terms of M and  $r/\sqrt{N}$ . Note that the values of M and  $r/\sqrt{N}$  do not seem to be sensitive to the resolution of the drop, although results from more ratios of  $D/\Delta$  (where  $\Delta$  denotes the grid spacing) will be necessary to confirm this. Again, the difference between the errors from the case of the drop advected with an imposed velocity and those from the case of the drop advected by the solution of the N-S equations does not seem to be significant. These observations support the hypothesis that M and thus  $r/\sqrt{N}$  are functions of only the grouping criterion for sufficiently well-resolved drops (or bubbles). Since Schemes B and C appear to provide reasonable support for  $r/\sqrt{N}$  ( $\lesssim$  100) in realistic grids with an appropriate threshold choice and do not preserve long and thin air bridges (see Table 1), which are typically poorly resolved, most of the subsequent discussion will be focused on these two schemes.

# 2.4. Comparison of algorithms: breaking wave

The various grouping schemes are now applied to the identification of bubbles in an ensemble of simulations of breaking waves to determine the influence of the errors of the various schemes on the computation of bubble size distributions in a turbulent flow. 30 simulations of a breaking third-order Stokes wave (air-water) with the dimensionless parameters  $We = 1.6 \times 10^3$  and  $Re = 1.8 \times 10^5$  were performed for this test. Using the wavelength L as the characteristic length scale, and the corresponding deep water wave velocity  $u_L = \sqrt{gL/2\pi}$  as the characteristic velocity scale corresponding to this length scale, the Weber and Reynolds numbers of the wave may be defined as  $We = \rho_l u_L^2 L/\sigma$  and  $Re = \rho_l u_L L/\mu_l$ , respectively. Here,  $\rho_l$ ,  $\mu_l$  and  $\sigma$  are the liquid density and viscosity, and the liquid-gas surface tension coefficient, respectively. The computational

Scheme	$M (D/\Delta = 8)$	$r/\sqrt{N} \ (D/\Delta = 8)$	$M (D/\Delta = 16)$	$r/\sqrt{N} \ (D/\Delta = 16)$
В1	0.1	1	0.1	1
B2	0.01	4	0.01	4
С	$5 \times 10^{-4}$	20	$2 \times 10^{-4}$	30
D	Less than m.p.	1/(Less than m.p.)	Less than m.p.	1/(Less than m.p.)

Table 5. Values of M and r as defined in Eqs. (2.2) and (2.5), respectively, for the case of the drop advected by the solution of the N-S equations. Refer to the caption of Table 2 for the definitions of the symbols and schemes. Here, m.p. denotes machine precision, and "less than m.p." indicates that the computed coefficient is associated with a value less than the standard double precision machine epsilon  $\sim 10^{-16}$ . The relative diameter error for each drop and scheme may be obtained by substituting M into Eq. (2.3).

mesh consisted of about 4.2 million mesh nodes, the minimum grid spacing  $\Delta_{\min}$  was L/216, and the length of the computational domain along each Cartesian axis was L. The mesh is nonuniform and is coarser closer to the edges of the domain in the wave-normal direction, such that a large majority of the generated bubbles are resolved with the minimum grid spacing. The wave steepness, which is the product of the wave amplitude and the fundamental wavenumber  $2\pi/L$ , was 0.55, and the corresponding initial velocity field was documented by Iafrati (2009). Periodic boundary conditions were employed in the directions parallel to the interface, and slip boundary conditions were employed in the wave-normal direction. Since the flow under consideration is statistically unsteady, ensemble averaging is more appropriate than time averaging for obtaining flow statistics. Using the timescale  $T = \sqrt{g/L}$  such that the first impact occurs just after  $t^* = t/T =$ 1, ensemble-averaged bubble size distributions generated with various grouping criteria in the flood-fill algorithm are plotted at  $t^* = 2.5$  and  $t^* = 4.0$  in Figures 3 and 4, respectively. The nondimensional radius bin sizes used to compute the size distributions were selected such that they were on the order of, if not smaller than, the nondimensional radius errors corresponding to the volume errors predicted in Section 2.3, as demonstrated in Table 6. Under this constraint, sensitivity of the shapes of the distributions to the choice of the bin size was not observed. Some observations on the size distributions are in order here. First, the choice of the grouping criterion greatly influences the power laws that result from the distributions. Care should thus be taken in interpreting power laws from distributions generated using grouping criteria that result in large volume errors. Second, the distributions from the application of no clipping (Scheme A,  $\phi_c = 0$ ) exhibit large variances in their data, suggesting the large influence of spurious bubbles on the distributions. Third, the distributions from the application of limited clipping (Scheme B2,  $\phi_c = 0.1$ ) and the substantial mass test (Scheme C, here with  $\phi_{c,m} =$ 0.5) are mostly indistinguishable, with significant variations still present in the data at large radii, suggesting that the difference in volume error inherent in the schemes as investigated in Section 2.3 is as significant as the difference in the way the schemes treat anisotropic, nonspherical bubbles with thin air bridges connecting large air masses. An example of such a bubble is depicted in Figure 5. Work is ongoing to develop methods that consistently deal with these anisotropic bubbles in a grid-independent fashion.

Scheme	B1	B2	С	Bin size
Nondimensional radius error or interval	$4 \times 10^{-4}$	$5\times10^{-5}$	$9\times10^{-7}$	$2 \times 10^{-4}$

Table 6. Errors in the nondimensional bubble radius due to the volume errors incurred by the various grouping criteria used in the bubble identification algorithm as discussed in Section 2.3, in comparison with the size of the bin in nondimensional radius space containing the nondimensional minimum grid size  $\Delta_{\min}/L$  (depicted by a dotted vertical line in Figures 3 and 4). Refer to the caption of Figure 3 for a description of the various schemes. Here, Scheme C (substantial mass test) is implemented with  $\phi_{c,m}=0.5$ . The errors are computed using Eq. (2.2) and the values of M listed in Table 4. This is the limiting case since the bin size selected in this work increases exponentially with nondimensional radius, while the nondimensional radius error only increases weakly with nondimensional radius [e.g., by considering the leading-order error term in the series truncation approximation used to construct Eq. (2.2)], and may otherwise be approximated as  $M\Delta_{\min}/L$  [see, e.g., Eq. (2.3)].

#### 3. Bubble tracking algorithm for breakup and coalescence detection

The bubble identification algorithm discussed in Section 2 enables the computation of bubble size distributions in numerical simulations of two-phase flows, such as the breaking wave simulations described in Section 2.4. While this will be discussed in greater detail in the companion brief (Chan et al. 2018b), it is evident from Figures 3 and 4 that these bubble size distributions evolve dramatically as the flow progresses. The bubble identification algorithm alone, however, does not enable the computation of transfer fluxes within these distributions in size (radius or diameter) space, as each distribution is computed at a single time instant. Further physical insights may be obtained by analyzing the evolution of these distributions in time, which may be achieved by a bubble tracking algorithm that keeps a tally of the number of bubbles in the system over time and traces the lineage of each bubble. The continuation of bubbles, as well as the occurrence of breakup and coalescence events, can be determined through the application of a constraint demanding the satisfaction of the conservation of mass. This constraint needs to be supplemented with the knowledge that the simulation satisfies the Courant-Friedrichs-Lewy (CFL) condition, as well as a good understanding of the errors incurred by the bubble identification algorithm described in Section 2. Access to the conservative volume fraction field allows reliance on the principle of mass conservation, obviating the need to rely on contour reconstruction (Li et al. 2008) or multiple-hypothesis tracking (Jaqaman et al. 2008). These constraints will now be discussed.

#### 3.1. Constraints that should be satisfied during bubble breakup and coalescence

As a bubble travels within the domain, its mass (and thus volume in an incompressible setting) remains constant from one flow snapshot to another even if it deforms. Even if the bubble breaks up into two, or if two bubbles coalesce into one, the principle of mass conservation is necessarily satisfied before and after the change in topology. Suppose bubble #0 breaks up into bubbles #1 and #2 (or #1 and #2 coalesce to form #0). Then, the volumes  $V_i$  of the bubbles satisfy

$$V_0 = V_1 + V_2. (3.1)$$

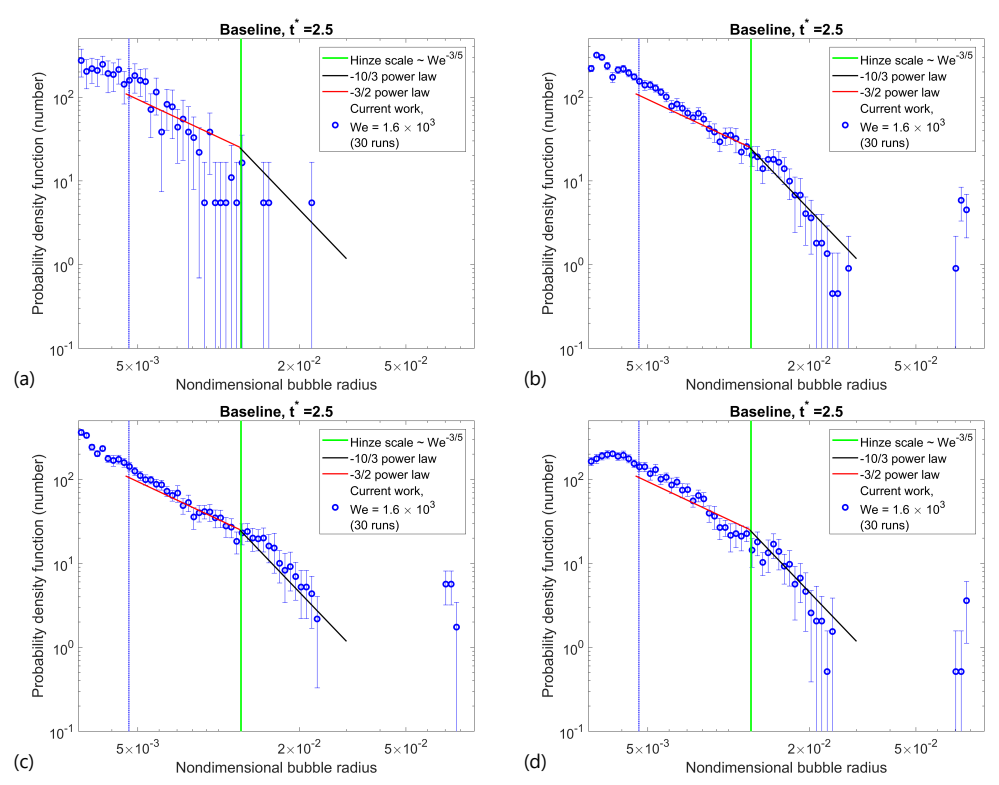


FIGURE 3. Ensemble-averaged bubble size distributions from 30 simulations of a breaking Stokes wave ( $t^* = 2.5$ ). Wave parameters are detailed in the main text. The grouping criteria used to generate the distributions are the original criterion in Section 2.1 (a, Scheme A), clipping with  $\phi_c = 0.5$  (c, Scheme B1), clipping with  $\phi_c = 0.1$  (d, Scheme B2) and the substantial mass test (Scheme C) with  $\phi_{c,m} = 0.5$  (b). The dotted vertical line to the left denotes the grid resolution, while the solid vertical line to the right denotes the estimated Hinze scale, which will be discussed in the companion brief (Chan et al. 2018b). The power-law fits will also be discussed by Chan et al. (2018b). The error bars denote the 95% confidence interval over the ensemble for each bubble size bin.

By the definition of the center of mass, the centroids  $\vec{x}_i$  of the bubbles also satisfy, just before  $(t_E^-)$  and after  $(t_E^+)$  the moment of breakup or coalescence  $t_E$ ,

$$\vec{x}_0(t_E^{\pm})V_0 = \vec{x}_1(t_E^{\pm})V_1 + \vec{x}_2(t_E^{\pm})V_2. \tag{3.2}$$

Now, consider a continuing bubble, i.e., a bubble that does not break up or coalesce between two flow snapshots n and n+1. Because of the volume error  $\Delta V_{\rm err}$  associated with the bubble identification algorithm, which were discussed in Section 2.3, the volume of a continuing bubble does not remain exactly the same between snapshots. Denote the volume of a bubble at a flow snapshot j as  $V^j$ . Then,  $V^j$  satisfies

$$\left| V^n - V^{n+1} \right| < \Delta V_{\text{err}}. \tag{3.3}$$

If the numerical simulation satisfies the CFL condition, then each fluid-fluid interface cannot traverse more than a single cell width in a single time step, multiplied by the maximum permissible Courant number for the advection scheme adopted in the simulation. It then follows that the centroid of the bubble remains stationary insofar as the permissible distance error is the product of the local grid cell spacing  $\Delta x$ , the number

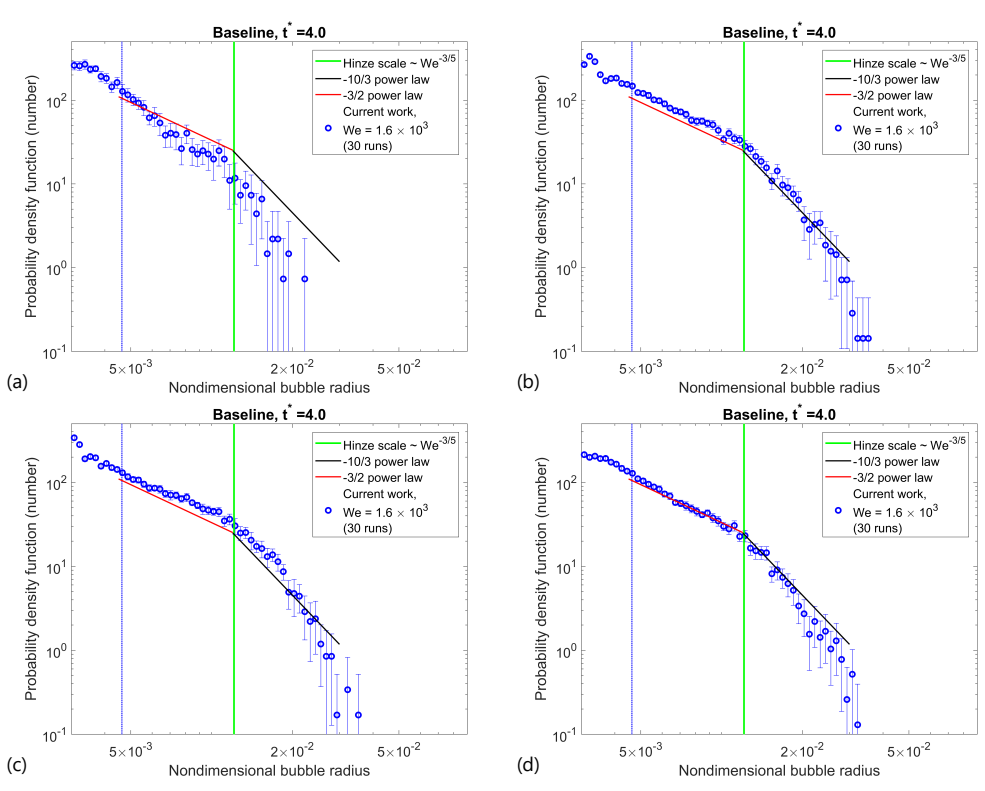


FIGURE 4. Ensemble-averaged bubble size distributions from 30 simulations of a breaking Stokes wave ( $t^* = 4.0$ ). Wave parameters are detailed in the main text, and the corresponding grouping criteria and other details are described in the caption of Figure 3.

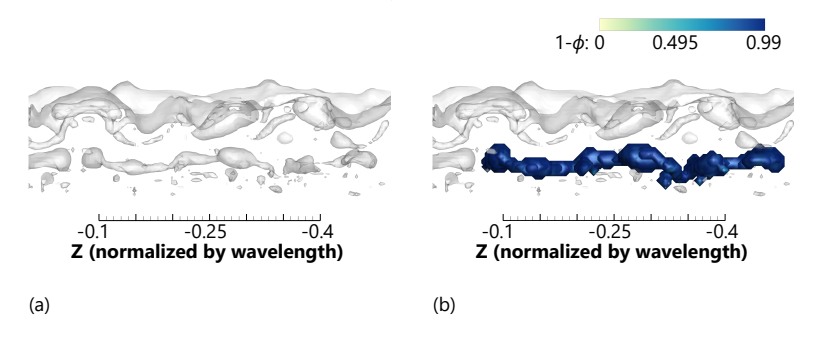


FIGURE 5. Example of an anisotropic, nonspherical bubble identified by a refined grouping algorithm (substantial mass test grouping criterion, Scheme C with  $\phi_{c,m}=0.5$ ) at  $t^*=3.6$ . (a) A portion of the  $\phi=0.5$  isosurface looking into the wave in the streamwise direction from a section cut. (b) The same portion with the identified bubble highlighted and its perimeter nodes shaded with the local water volume fraction in a fashion similar to the spurious bubble in Figure 2. For the scale bars, z refers to the spanwise coordinate.

of time steps  $N_t$  between the snapshots being considered, and the Courant number C adopted in the simulation. Denote the centroid of a bubble at a flow snapshot j as  $\vec{x}^j$ .

Then,  $\vec{x}^j$  satisfies

$$\left| \left| \vec{x}^n - \vec{x}^{n+1} \right| \right| < CN_t \Delta x. \tag{3.4}$$

Note that the bubble identification algorithm also generates spatial errors in the centroid location. However, as shown in Tables 2 and 3, the spatial errors associated with the identification algorithm are typically much smaller than the grid spacing, and will be neglected here.

One may now use Eqs. (3.3) and (3.4) to construct the discrete equivalents of Eqs. (3.1) and (3.2). Consider, first, the constraint arising from the principle of mass conservation. In the case of breakup, one may write

$$|V_0^n - [V_1^{n+1} + V_2^{n+1}]| < \Delta V_{\text{err}},$$
 (3.5)

while in the case of coalescence, one may write

$$\left| V_0^{n+1} - \left[ V_1^n + V_2^n \right] \right| < \Delta V_{\text{err}}. \tag{3.6}$$

Now, consider the constraint arising from the satisfaction of the CFL condition. In the absence of volume errors, one may write, for breakup, the following exact bound

$$\left\| \vec{x}_0^n - \frac{\vec{x}_1^{n+1} V_1^{n+1} + \vec{x}_2^{n+1} V_2^{n+1}}{V_1^{n+1} + V_2^{n+1}} \right\| < C N_t \Delta x, \tag{3.7}$$

while in the case of coalescence, one may write

$$\left\| \vec{x}_0^{n+1} - \frac{\vec{x}_1^n V_1^n + \vec{x}_2^n V_2^n}{V_1^n + V_2^n} \right\| < C N_t \Delta x. \tag{3.8}$$

These bounds are approximate when the volume errors  $\Delta V_{\rm err}$  in Eqs. (3.5) and (3.6) are nonzero.

These constraints are sufficient for the identification of breakup and coalescence events, as well as continuing bubbles, using the bubble volumes and centroid locations. Note, however, that Tables 4 and 5 suggest that there is a critical size ratio r—substituting the appropriate value for N for each bubble pair—above which breakup and coalescence events involving a small bubble and a large bubble cannot be distinguished from fluctuations in the volume of the large bubble from one snapshot to another. Choosing a bubble identification scheme with a lower volume error increases this critical size ratio keeping the resolution of the smallest bubble constant, allowing more breakup and coalescence events to be captured accurately.

# 3.2. Identifying bubble breakup and coalescence events by tracking centroid locations and bubble volumes

In order to identify breakup and coalescence events, individual bubbles must be tracked through time. The bubble tracking algorithm proposed in this work involves comparing lists of bubble volumes and centroids from two consecutive flow snapshots separated by a time interval  $N_t\Delta t$ , where  $\Delta t$  is the time step adopted in the simulation. This process of analyzing pairs of snapshots is successively repeated from the first to the penultimate snapshot to obtain a family tree of bubbles throughout the flow evolution. First, the two lists are traversed in order to locate and tag continuing bubbles. Continuing bubbles are identified through the satisfaction of Eqs. (3.3) and (3.4). This search for continuing bubbles incurs a computational cost  $O(N_b^2)$ , where  $N_b$  is the higher number of bubbles in both lists. Then, the remaining untagged (non-continuing) bubbles are tested for breakup

and coalescence events using the constraints in Eqs. (3.5)–(3.8). This search among noncontinuing bubbles incurs a computational cost  $O(n_b^3)$ , where  $n_b \lesssim N_b$  is the higher number of noncontinuing bubbles in both lists. To avoid excessive computational costs, a sufficiently small  $N_t$  should be chosen so that  $n_b \ll N_b$ . Finally, in order to account for the edge case of large-size-ratio breakup and coalescence events involving one large bubble and one small bubble, where the large bubble may have been identified as continuing in the first traversal, the lists are looped over one final time to locate these events. This is done using the constraints in Eqs. (3.5)–(3.8) under the following restrictions: either the continuing bubble is identified as bubbles #0 and #2 and the non-continuing bubble is identified as bubble #1, or the continuing bubble is identified as bubbles #0 and #1 and the non-continuing bubble is identified as bubble #2. If such an event is determined to have occurred, then the large bubble is no longer tagged as continuing, and the three participating bubbles are reclassified as being part of a breakup or coalescence event instead. This search, which requires one loop over the set of continuing bubbles and one loop over the set of non-continuing bubbles, incurs a computational cost  $O(N_h n_h)$ . All remaining bubbles are then associated with birth (new bubble appears) or death (existing bubble disappears) events. In the case where the total volume of the bubbles remains constant with no inflow or outflow of air, the presence of birth and death events would suggest that breakup and coalescence events might have been missed due to the errors discussed above (e.g., large-size-ratio events), the occurrence of ternary/polyadic breakup or coalescence, or the occurrence of successive breakup or coalescence events involving the same bubble(s) that were mixed up due to the finite time interval between the snapshots. The presence of these birth and death events explicitly indicates the failure of the algorithm to capture relevant breakup and coalescence events. The case of inflow and/or outflow of air requires more careful consideration of the birth and death of bubbles and will not be discussed in this brief. An illustration of this algorithm is provided in Figure 6.

#### 3.3. Demonstration of the algorithm

The algorithm will now be demonstrated on the breakup of a drop in a two-dimensional (2D) freely-decaying Taylor-Green vortex with  $\nu_d/\nu_c = 5$  and  $We_D = 20$ , where  $\nu$  denotes the kinematic viscosity, d and c denote the dispersed and carrier phases, respectively, and  $We_D$  denotes the Weber number based on the droplet diameter D and carrier fluid conditions. More detailed parameters of this test case are outlined in the caption of Figure 7. Other test cases, such as the coalescence of many drops (Chan et al. 2017) and breakup/coalescence events in more highly-strained single drops breaking up in more energetic Taylor-Green vortices ( $\nu_d/\nu_c=1$  and higher  $Re_D$  with comparable  $\rho_d/\rho_c$  and  $We_D$ , where  $Re_D$  denotes the Reynolds number based on the droplet diameter and carrier fluid conditions, and  $\rho$  denotes density), have been omitted for brevity. Figure 7 depicts snapshots of the drop in the vortex before and after breakup, while Figure 8 shows the breakup events detected using different time intervals between snapshots. In the case of the shorter time interval, all the breakup events are recovered; in the case of the longer time interval, some breakup events are missed since more than one breakup occurs in some of the intervals. The remaining event is unaltered, suggesting that a longer time interval between snapshots only misses events and does not distort the nature of the remaining detectable events.

In the interest of space, as well as anticipation of a more careful discussion of an appropriate time interval between snapshots in relation to expected breakup and coales-

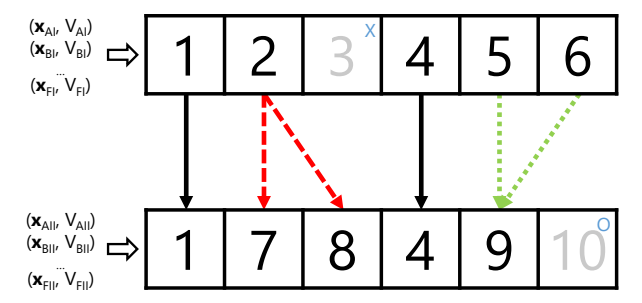


FIGURE 6. An illustration of the bubble tracking algorithm described in Section 3.2. As depicted on the left of the figure, the algorithm requires two lists of bubbles: the list in the top row corresponds to the bubbles present in some flow snapshot (I), while the list in the bottom row corresponds to the bubbles present in the succeeding snapshot (II). In this example, each list contains six bubbles (labeled A–F) in both snapshots. No relation between the two sets of six bubbles is assumed a priori. The algorithm takes the centroid and volume of each bubble as inputs. The two rows of cells on the right of the figure depict the same lists after the algorithm has been executed, and the numbers in each list entry correspond to the tags assigned to each bubble. Suppose the bubbles in the first snapshot were assigned the tags #1–#6. The solid arrows indicate that bubbles #1 and #4 are continuing. The dashed arrows indicate that bubble #2 split up into bubbles #7 and #8. The dotted arrows indicate that bubbles #5 and #6 coalesced to form bubble #9. Because bubble #3 could not be associated with a bubble in the second list, its disappearance should be associated with a death event ( $\times$ ), and because bubble #10 could not be associated with a bubble in the first list, its formation should be associated with a birth event ( $\circ$ ).

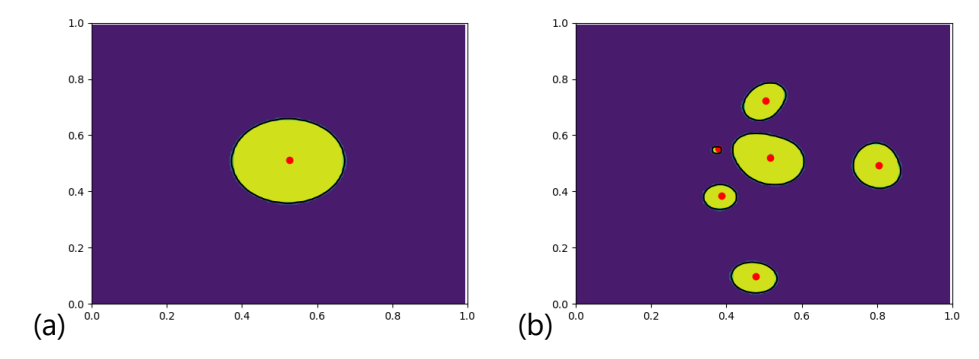


FIGURE 7. Snapshots of drop breakup in a 2D Taylor-Green vortex, before (a) and after (b) breakup. The contrasting colors denote different phases, and the small dots indicate the centroids of each drop. The snapshots are separated by 2560 time steps. Here, the Reynolds and Weber numbers of the system based on the drop diameter and carrier fluid conditions are  $Re_D = 300$  and  $We_D = 20$ , respectively, while the density and viscosity ratios of the dispersed phase to the carrier phase are  $\rho_d/\rho_c = 5$  and  $\nu_d/\nu_c = 5$ , respectively.

cence frequencies, the demonstration of the algorithm on the breaking wave introduced in Section 2.4 is deferred to the companion brief (Chan *et al.* 2018b).

#### 4. Conclusions

This work has developed algorithms enabling the computation of bubble size distributions, and the identification of bubble breakup and coalescence events via the tracing of

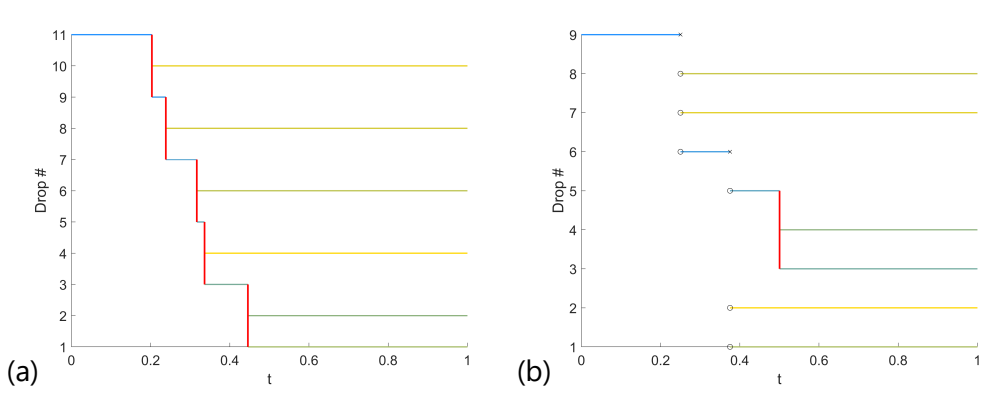


FIGURE 8. Family tree of drops constructed by the algorithm in Section 3.2 for the breakup depicted in Figure 7 where the time interval between snapshots is 10 time steps (a) / 160 time steps (b). The drop tags (vertical axis) and time units (horizontal axis) are arbitrary. Each horizontal line depicts a drop, and adopts a color between blue (largest drop, darker in grayscale) and yellow (smallest drop, lighter in grayscale) that is visible in the online version of this brief. The colors of these lines are not essential to the interpretation of the trees. The vertical lines depict breakup, where the parent drop is to the left and the child drops are to the right of each vertical line. The circles denote birth events and the crosses denote death events, consistent with the symbols introduced in Figure 6.

bubble lineages. The computation of bubble size distributions involves the identification of the volumes of individual bubbles, which may be accomplished by the flood-fill algorithm. The flood-fill algorithm relies on a grouping criterion that determines whether pairs of cells should be included in a group. Several grouping criteria were explored in this work in order to reduce the influence of spurious numerical bubbles without incurring excessive volume errors. Application of the various schemes to the simple test case of a moving drop suggests that clipping is not suitable as a grouping criterion unless the threshold value  $\phi_c$  selected is sufficiently small due to the incurred volume errors. Once this is satisfied, the resultant bubble size distribution in more complex flows is virtually indistinguishable from that generated by the substantial mass test, although clipping introduces a larger volume error in individual bubbles. It should be noted that these errors may be corrected in the sense of the mean. Sensitivity of the observations in Sections 2.3 and 2.4 to the threshold values  $\phi_c$ ,  $\phi_{c,m}$ , and  $\phi_{c,n}$  will need to be investigated further in future work, as will anisotropic bubbles that have a grid-dependent effect on the distributions. The identification of bubble breakup and coalescence events relies on the computation of bubble volumes and centroid locations, in tandem with the enforcement of the constraints that the bubbles satisfy the conservation of mass, and that the simulation satisfies the CFL condition. With these constraints, as well as a good handle on the errors incurred by the bubble identification algorithm, lists of bubbles from consecutive snapshots may be compared and tested for these events. Opportunities for improvement of this algorithm include its inherent inability to identify large-size-ratio events, as well as ternary/polyadic breakup and coalescence events arising from actual ternary/polyadic interactions or from the finite time interval between consecutive snapshots. The invariance of the resulting statistics to the duration between consecutive snapshots will also need to be investigated further in future work.

#### Acknowledgments

This investigation was funded by the Office of Naval Research, Grant #N00014-15-1-2726. W. H. R. Chan is also funded by a National Science Scholarship from the Agency of Science, Technology and Research in Singapore. The authors acknowledge computational resources from the U.S. Department of Energy, as well as from the Certainty cluster awarded by the National Science Foundation to CTR.

#### REFERENCES

- BARALDI, A., DODD, M. S. & FERRANTE, A. 2014 A mass-conserving volume-of-fluid method: Volume tracking and droplet surface-tension in incompressible isotropic turbulence. *Comput. Fluids* **96**, 322–337.
- BLENKINSOPP, C. E. & CHAPLIN, J. R. 2010 Bubble size measurements in breaking waves using optical fiber phase detection probes. *IEEE J. Ocean Eng.* **35**, 388–401.
- Chan, W. H. R., Urzay, J., Mani, A. & Moin, P. 2016 On the development of a subgrid-scale model for the generation of micro-bubbles from impacting liquid surfaces. *Annual Research Briefs*, Center for Turbulence Research, Stanford University, pp. 149–162.
- Chan, W. H. R., Urzay, J. & Moin, P. 2017 Development of a collision detection algorithm for complex two-phase flows. *Annual Research Briefs*, Center for Turbulence Research, Stanford University, pp. 103–116.
- Chan, W. H. R., Urzay, J. & Moin, P. 2018a Subgrid-scale modeling for microbubble generation amid colliding water surfaces. *Proceedings of the 32nd Symposium on Naval Hydrodynamics*, Hamburg, Germany.
- Chan, W. H. R., Dodd, M. S., Johnson, P. L., Urzay, J. & Moin, P. 2018b Formation and dynamics of bubbles in breaking waves: Part II. The evolution of the bubble size distribution and breakup/coalescence statistics. *Annual Research Briefs*, Center for Turbulence Research, Stanford University, pp. 21–34.
- CROOK, J. A., JACKSON, L. S. & FORSTER, P. M. 2016 Can increasing albedo of existing ship wakes reduce climate change? *J. Geophys. Res. Atmos.* 121, 1549–1558.
- Deane, G. B. & Stokes, M. D. 2002 Scale dependence of bubble creation mechanisms in breaking waves. *Nature* 418, 839–844.
- Deike, L., Melville, W. K. & Popinet, S. 2016 Air entrainment and bubble statistics in breaking waves. *J. Fluid Mech.* **801**, 91–129.
- Fuster, D., Arrufat, T., Crialesi-Esposito, M., Ling, Y., Malan, L., Pal, S., Scardovelli, R., Tryggvason, G. & Zaleski, S. 2018 A momentum-conserving, consistent, Volume-of-Fluid method for incompressible flow on staggered grids. arXiv:1811.12327.
- IAFRATI, A. 2009 Numerical study of the effects of the breaking intensity on wave breaking flows. J. Fluid Mech. 622, 371–411.
- Jaqaman, K., Loerke, D., Mettlen, M., Kuwata, H., Grinstein, S., Schmid, S. L. & Danuser, G. 2008 Robust single-particle tracking in live-cell time-lapse sequences. *Nat. Methods* 5, 695–702.
- KIM, D., HAM, F., BOSE, S., LE, H., HERRMANN, M., LI, X., SOTERIOU, M. C. & KIM, W. High-fidelity simulation of atomization in a gas turbine injector high shear nozzle. ILASS Americas 26th Annual Conference, Portland, OR, USA, May 2014.
- LI, K., MILLER, E. D., CHEN, M., KANADE, T., WEISS, L. E. & CAMPBELL, P. G.

- 2008 Cell population tracking and lineage construction with spatiotemporal context. *Med. Image Anal.* **12**, 546–566.
- Melville, W. K. 1996 The role of surface-wave breaking in air-sea interaction. *Annu. Rev. Fluid Mech.* **28**, 279–321.
- Pumphrey, H. C. & Crum, L. A. 1988 Acoustic emissions associated with drop impacts. In Sea Surface Sound: Natural Mechanisms of Surface-Generated Noise in the Ocean, ed. B. R. Kerman, pp. 463–483. Kluwer Academic Publishers.
- REED, A. M. & MILGRAM, J. H. 2002 Ship wakes and their radar images. *Annu. Rev. Fluid Mech.* **34**, 469–502.
- Scardovelli, R. & Zaleski, R. 2003 Interface reconstruction with least-square fit and split Eulerian-Lagrangian advection. *Int. J. Numer. Meth. Fl.* 41, 251–274.
- Seitz, R. 2011 Bright water: hydrosols, water conservation and climate change. *Climatic Change* **105**, 365–381.
- STANIC, S., CARUTHERS, J. W., GOODMAN, R. R., KENNEDY, E. & BROWN, R. A. 2009 Attenuation measurements across surface-ship wakes and computed bubble distributions and void fractions. *IEEE J. Ocean Eng.* **34**, 83–92.
- TERRILL, E. J., MELVILL, W. K. & STRAMSKI, D. 2001 Bubble entrainment by breaking waves and their influence on optical scattering in the upper ocean. *J. Geophys. Res.* **106**, 16815–16823.
- Thorpe, S. A. 1992 Bubble clouds and the dynamics of the upper ocean. Q. J. Roy. Meteor. Soc. 118, 1–22.
- TREVORROW, M. V., VAGLE, S. & FARMER, D. M. 1994 Acoustical measurements of microbubbles within ship wakes. *J. Acoust. Soc. Am.* **95**, 1922–1930.
- Wang, Z., Yang, J. & Stern, F. 2016 High-fidelity simulations of bubble, droplet and spray formation in breaking waves. *J. Fluid Mech.* **792**, 307–327.
- WEYMOUTH, G. D. & YUE, D. K.-P. 2010 Conservative Volume-of-Fluid method for free-surface simulations on Cartesian-grids. *J. Comp. Phys.* **229**, 2853–2865.
- ZHANG, X., LEWIS, M., BISSETT, W. P., JOHNSON, B. & KOHLER, D. 2004 Optical influence of ship wakes. *Appl. Optics* 43, 3122–3132.